A globally conforming method for solving flow in discrete fracture networks using the Virtual Element Method

A GLOBALLY CONFORMING METHOD FOR SOLVING FLOW IN DISCRETE FRACTURE NETWORKS USING THE VIRTUAL ELEMENT METHOD *

MATÍAS FERNANDO BENEDETTO†, STEFANO BERRONE†, AND STEFANO SCIALÒ†

April 23, 2015

Abstract. A new approach for solving flow in Discrete Fracture Networks (DFN) is developed in this work by means of the Virtual Element Method. Taking advantage of the features of the VEM, we obtain global conformity of all fracture meshes while preserving a fracture-independent meshing process. This new approach is based on a generalization of globally conforming Finite Elements for polygonal meshes that avoids complications arising from the meshing process. The approach is robust enough to treat many DFNs with a large number of fractures with arbitrary positions and orientations, as shown by the simulations. Higher order Virtual Element spaces are also included in the implementation with the corresponding convergence results and accuracy aspects.

Key words. VEM, Fracture flows, Darcy flows, Discrete Fracture Networks

AMS subject classifications. 65N30, 65N15, 65N50, 65J15

1. Introduction. The present work deals with a new approach based on the Virtual Element Method (VEM) for the simulation of the flow in Discrete Fracture Networks (DFNs). DFN models are one of the possible approaches for simulating subsurface flows and they consist of a set of planar polygons in 3D space resembling the fractures in the underground. Each fracture is modelled individually, as opposed to continuum models with equivalent porosity, and, for geological formations with sparse fracture network that mainly affect the flow path, this approach is recommended [1, 19]. DFNs are used in a wide range of applications such as pollutant percolation, gas recovery, aquifers, reservoir analysis, among others [26] [16].

Stationary flow in a DFN is modelled using Darcy's law and introducing a transmissivity tensor for each fracture that depends on its aperture and its resistance to flow. The surrounding rock matrix is considered impervious. The goal is to obtain the hydraulic head distribution in the system, which is the sum of the pressure head and the elevation. Fluid can only flow through fractures and across intersections between fractures, also called traces, but no tangential flow is considered along traces. The hydraulic head is a continuous function, but with discontinuous derivatives across the traces, which act as sources/sinks of flow. Since little is known about the subsurface fractures, stochastic models are used in order to determine distributions of aperture, hydrological properties, size, orientation, density, and aspect ratio of the fractures.

Geometrical complexity is the greatest challenge when dealing with DFN-based simulations. Since the fracture generation has a random component, many complex situations arise that render the meshing process very complicated and sometimes impossible, e.g. very small angles, very close and almost parallel traces, high disparity of traces lengths, etc. In order to use traditional finite elements, fracture grids have to match in all the intersections between fractures, since these are discontinuity interfaces for the first order derivatives of the solution. All the mentioned geometrical

*This research has been partially supported by the Italian MIUR through PRIN research grant 2012HBLYE4_001 *Metodologie innovative nella modellistica differenziale numerica* and by INdAM-GNCS through project *Tecniche numeriche per la simulazione di flussi in reti di fratture di grandi dimensioni*.

†Dipartimento di Scienze Matematiche, Politecnico di Torino, Corso Duca degli Abruzzi 24, 10129 Torino, Italy. e-mail: {matias.benedetto,stefano.berrone, stefano.scialo}@polito.it

configurations complicate the meshing process and are the biggest obstacle in the discretization of the problem because it becomes very computationally demanding to obtain a good mesh from such a badly predisposed geometry. Furthermore, the meshing procedure depends on the whole DFN and is not independent for each fracture. When a large DFN is considered that can have thousands of fractures, mesh conformity requirements can lead to a very high number of elements that are far more than those demanded by the required level of accuracy. In [23], a BEM (Boundary Element Method) was applied that aims to minimize core memory usage by defining and storing only a relation between nodal fluxes and hydraulic head on traces for each fracture. The problem of obtaining a good globally conforming mesh is the subject of ongoing research. In [24], an adaptive mesh refinement method is described that aims for a high resolving mesh. Previous works [20, 29] suggest a simplification of the geometry to ease meshing. Monodimensional pipes joining fractures, instead of traces, have been put forward as an alternative in [13] and [17]. In [25], a mixed formulation and a mesh modifying procedure was used to solve DFNs and reducing the number of elements for each fracture. Another mixed formulation was used in [18], where local corrections of traces are applied in order to obtain a globally conforming mesh. The mortar method was used to impose conditions between fractures with non-matching grids to obtain a mixed hybrid formulation in [27], with a subsequent generalization in [28] that includes trace intersections within a fracture. A novel approach was proposed in [9], [10] and [11] in which the problem was reformulated as a PDE-constrained optimization. The minimization of a properly defined functional is adopted to enforce fluid flow continuity and conservation at fracture intersections. Traditional finite elements (FEM) as well as extended finite elements (XFEM) were implemented to solve the problem.

In this work, we aim to provide an easy, natural way for generating conforming meshes for complex DFN problems using the VEM. The proposed approach is a generalization of traditional conforming finite elements, keeping the method as simple and streamlined as possible. Some of the ideas presented here where present in a previous work by the authors [8], that introduced Virtual Elements (VEM) to DFNs. We make absolutely no assumptions on the meshing procedure, which is done independently for each fracture and without any consideration of the position of the traces. Traces are not modified in any way, and using some of the features of the VEM, local and global conformity for the mesh is obtained by means of splitting the original elements of the meshes independently generated on each fracture into polygons of an arbitrary number of vertices.

Using Lagrange multipliers we obtain a hybrid system that can be solved with different methods, including FETI algorithms for domain decomposition.

Section 2 provides the formulation of the DFN problem in the present context, whereas a brief summary of the VEM is reported in Section 3, and in Section 4 the proposed method is described in detail. Numerical results are presented in Section 5, where some convergence results are given and the applicability of the method to DFNs is discussed.

2. The continuous problem. Let us consider a set of open convex planar polygonal fractures $F_i \subset \mathbb{R}^3$ with $i = 1, ..., N$, with boundary ∂F. Our DFN is $\Omega = \bigcup_i F_i$, with boundary $\partial\Omega$. Even though the fractures are planar, their orientations in space are arbitrary, such that Ω is a 3D set. The set $\Gamma_D \subset \partial\Omega$ is where Dirichlet boundary conditions are imposed, and we assume $\Gamma_D \neq \emptyset$, whereas $\Gamma_N = \partial\Omega \setminus \Gamma_D$, is the portion of the boundary with Neumann boundary conditions. Dirichlet and

Neumann boundary conditions are prescribed by the functions $h^D \in \mathrm{H}^{\frac{1}{2}}(\Gamma_D)$ and $g^N \in \mathrm{H}^{-\frac{1}{2}}(\Gamma_N)$ on the Dirichlet and Neumann part of the boundary, respectively. We further set $\Gamma_{iD} = \Gamma_D \cap \partial F_i$, $\Gamma_{iN} = \Gamma_N \cap \partial F_i$, and $h_i^D = h^D{}_{|\Gamma_{iD}}$ and $g_i^N = g^N{}_{|\Gamma_{iN}}$. The set $\mathcal{T}$ collects all the traces, i.e. the intersections between fractures, and each trace $T \in \mathcal{T}$ is given by the intersection of exactly two fractures, $T = \bar{F}_i \cap \bar{F}_j$, such that there is a one to one relationship between a trace T and a couple of fracture indexes $\{i, j\} = \mathcal{I}(T)$. We will also denote with $\mathcal{T}_i$ the set of traces belonging to fracture F_i.

Subsurface flow is governed by the gradient of the hydraulic head $H = \mathcal{P} + \zeta$, where $\mathcal{P} = p/(\varrho g)$ is the pressure head, p is the fluid pressure, g is the gravitational acceleration constant, ϱ is the fluid density and ζ is the elevation.

We define the following functional spaces:

$$V_i = \mathrm{H}^1_0(F_i) = \left\{ v \in \mathrm{H}^1(F_i) : v_{|\Gamma_{iD}} = 0 \right\},$$

$$V_i^D = \mathrm{H}^1_{\mathrm{D}}(F_i) = \left\{ v \in \mathrm{H}^1(F_i) : v_{|\Gamma_{iD}} = h_i^D \right\},$$

and

$$V = \left\{ v : v_{|F_i} \in V_i,\ \forall i = 1, \dots, N,\ \gamma_T(v_{|F_i}) = \gamma_T(v_{|F_j}),\ \forall T \in \mathcal{T}_i,\ \{i, j\} = \mathcal{I}(T) \right\},$$

where γ_T is the trace operator onto T. It is then possible to formulate the DFN problem, given by the Darcy's law in its weak form on the fractures with additional constraints of continuity of the hydraulic head across the traces: for $i = 1, \dots, N$, find $H_i \in V_i^D$ such that $\forall v \in V$

$$\int_{F_i} \mathcal{K}_i \nabla H_i \nabla v_{|F_i} \mathrm{d}F_i = \int_{F_i} f_i v_{|F_i} \mathrm{d}F_i + \langle G_N, v_{|\Gamma_{N_i}} \rangle_{\mathrm{H}^{-\frac{1}{2}}(\Gamma_{N_i}), \mathrm{H}^{\frac{1}{2}}(\Gamma_{N_i})},$$
$$\gamma_T(H_i) = \gamma_T(H_j),\ \forall T \in \mathcal{T},\ \{i, j\} = \mathcal{I}(T)$$

where $\mathcal{K}_i$ is the fracture transmissivity tensor, that we assume is constant on each fracture. The second equation represents the continuity of the hydraulic head across traces. We remark that, without loss of generality, assuming homogeneous Dirichlet boundary conditions, on each fracture the bilinear form $a_i : V_i \times V_i \mapsto \mathbb{R}$:

$$a_i(H_i, v_{|F_i}) = \int_{F_i} \mathcal{K}_i \nabla H_i \nabla v_{|F_i} \mathrm{d}F_i \tag{2.1}$$

is symmetric and coercive.

3. The Virtual Element Method. This section provides a quick overview of the VEM, recalling the main features useful in the present context. We refer the reader to the original paper [5] for a proper introduction and to [4] for a guide on implementation. Further developments can be found in [2], [14], [7] and [6]. The VEM has also been applied to problems in elasticity [15], plate bending [12], the Stokes problem [3] and has sparked interest in other applications as well.

Borrowing ideas from the Mimetic Difference method, the VEM can be regarded as a generalization of regular finite elements to meshes made up by polygonal elements of any number of edges. The discrete functional space on each element has, in general, not only polynomial functions but also other functions that are only known at a certain set of degrees of freedom. Given a bilinear form to be approximated with the VEM,

our goal is to build a discrete bilinear form that coincides with the exact one when at least one of the arguments is a polynomial. For the other cases, a rough approximation that scales in a desired way is enough for the convergence of the method.

Given a domain $F \subset \mathbb{R}^2$, a mesh τ_h on F, made of polygons $\{E\}$ with mesh parameter h (i.e. the square root of the maximum element area), and the space of the polynomials of maximum order k, $\mathcal{P}_k$, let us define the local space $V_{k,h}^E$ for a given polynomial accuracy k as:

$$V_{k,h}^E = \left\{ v_h \in H^1(E) : v_{h|\partial E} \in C^0(\partial E),\ v_{h|e} \in \mathcal{P}_k(e)\ \forall e \subset \partial E,\ \Delta v_h \in \mathcal{P}_{k-2}(E) \right\}$$

where ∂E is the border of E, and e an edge.

From the above definition it is clear that the space $\mathcal{P}_k(E)$ is a subset of $V_{k,h}^E$. We define the following degrees of freedom for each element E:

- The value of v_h at the vertices of E;
- The value of v_h at $k-1$ internal points on each edge of E;
- The moments $\frac{1}{|E|}\int_E v_h m_\alpha$ for $|\alpha| \leqslant k-2$,

where m_α, with $\alpha = (\alpha_1, \alpha_2)$, represent scaled monomials of the type

$$m_\alpha = (\frac{x - x_c}{h_E})^{\alpha_1} (\frac{y - y_c}{h_E})^{\alpha_2},$$

and (x_c, y_c) and h_E are the centroid and the diameter of the element E respectively. Different choices for the second type of degree of freedom is possible instead of point values, e.g. edge moments. We have chosen point values on Gauss-Lobatto nodes on edges for numerical integration purposes. The selected set of degrees of freedom is unisolvent [5], and therefore, given an element E with n_v vertices, we have that the dimension of $V_{k,h}^E$ is $\#V_{k,h}^E = n_v k + \frac{k(k-1)}{2}$. We finally choose a base for $V_{k,h}^E$, made of functions ϕ_i with $i = 1, ..., \#V_{k,h}^E$, such that, calling $\mathrm{dof}_j(v)$, for $j = 1, \ldots, \#V_{k,h}^E$ the j-th degree of freedom applied to v, we have $\mathrm{dof}_j(\phi_i) = \delta_{ij}$, being δ_{ij} the Kronecker delta. The global virtual element space is:

$$V_{k,h} = \left\{ v_h \in H^1(F) : v_h|_E \in V_{k,h}^E\ \forall E \in \tau_h \right\},$$

and we can easily check that the chosen degrees of freedom on the edges of each element allow to easily enforce continuity of any function $v_h \in V_{k,h}$ on the internal edges of the partition τ_h.

Let us now consider the restriction of the bilinear form (2.1) to a mesh element E, $a_i^E(.,.)$. We aim at building a discrete bilinear form $a_{i,h}^E : V_{k,h}^E \times V_{k,h}^E \mapsto \mathbb{R}$ having the previously stated polynomial consistency, i.e. the discrete bilinear form has to coincide with the exact one when at least one of the arguments is a polynomial of maximum degree k. To this end let us consider the projector operator of order k on E:

$$\Pi_{E,k}^\nabla : V_{k,h}^E \longrightarrow \mathcal{P}_k(E)$$

such that

$$\Pi_{E,k}^\nabla q_k = q_k \text{ for all } q_k \in \mathcal{P}_k(E),$$

defined by the equations

$$\int_E \nabla q_k \cdot \nabla v_h = \int_E \nabla q_k \cdot \nabla \Pi^{\nabla}_{E,k} v_h \text{ for all } q_k \in \mathcal{P}_k(E),$$
$$\int_E \Pi^{\nabla}_{E,k} v_h = \int_E v_h.$$

The projection $\Pi^{\nabla}_{E,k} v_h$ can be uniquely defined starting from the degrees of freedom of v_h using integration by parts [4] and represents an orthogonality condition in the H^1 inner product. The first equation defines the projection up to a constant, which is computed with the second equation. Other options for the second equation exist [6]. For order $k = 1$, it can be taken as

$$\frac{1}{|E|} \sum_{i=1}^{N^v} \Pi^{\nabla}_{E,k} v_h(\mathcal{V}_i) = \frac{1}{|E|} \sum_{i=1}^{N^v} v_h(\mathcal{V}_i).$$

where $\mathcal{V}_i$ are the vertices of the element and N^v its number.

REMARK 3.1. *In the case of a more complex equation than the Laplacian (or even the Laplacian with non-constant coefficients), other projectors have to be considered [6].*

Let us now take any symmetric, positive definite bilinear form $S^E_{i,h} : V^E_{k,h} \times V^E_{k,h} \mapsto \mathbb{R}$, such that there exist c_0 and c_1 positive constants, independent of the element E and its diameter, that verify

$$c_0 a^E(v_h, v_h) \leq S^E_{i,h}(v_h, v_h) \leq c_1 a^E(v_h, v_h) \quad \forall v_h \in V^E_{k,h} \text{ with } \Pi^{\nabla}_{E,k} v = 0.$$

This implies that $S^E_{i,h}$ *scales* like $a^E_i(v, v)$, and then the local discrete bilinear form $a^E_{i,h}$ is set as

$$a^E_{i,h}(u_h, v_h) = a^E_i(\Pi^{\nabla}_{E,k} u_h, \Pi^{\nabla}_{E,k} v_h) + S^E_{i,h}(u_h - \Pi^{\nabla}_{E,k} u_h, v_h - \Pi^{\nabla}_{E,k} v_h) \; \forall u_h, v_h \in V^E_{k,h},$$

The first terms ensures the *consistency* and the second one the *stability* of the form. Finally, the complete discrete bilinear form becomes

$$a_{i,h}(u_h, v_h) = \sum_{E \in \tau_h} a^E_{i,h}(u_h, v_h) \qquad \forall u_h, v_h \in V_{k,h}.$$

A possible choice for the bilinear form $S^E_{i,h}$ is the usual Euclidean product in $\mathbb{R}^{\#V^E_{k,h} \times \#V^E_{k,h}}$ between two vectors whose components are the values of the functions at the degrees of freedom. A stiffness matrix $\mathbf{K}_i$ is associated to the discrete bilinear form $a_{i,h}$, defined as :

$$(\mathbf{K}_i)_{pq} = a_{i,h}(\phi_q, \phi_p), \text{ for } p, q = 1, ..., \#V_{k,h}.$$

In general it is not true that the VEM stiffness matrix approximates the exact stiffness matrix as if it were computed numerically.

For the right hand side with load term f, it is enough for optimal convergence [4] to consider

$$(f, v) = \sum_{E \in \tau_h} \int_E f \Pi^0_{E,k-1} v \qquad \text{for order } k = 1, 2,$$

$$(f, v) = \sum_{E \in \tau_h} \int_E f \Pi^0_{E,k-2} v \qquad \text{for order } k \geq 3,$$

where $\Pi^0_{E,k}$ is the the full L^2 projection on the polynomials of degree k.

4. Problem implementation.

4.1. Mesh generation. Mesh generation is done independently for each fracture regardless of traces and their positions. The process of mesh generation consists of three steps: the first task is the generation of a baseline triangulation of each fracture, not necessarily conforming to trace disposition, and independent on each fracture; the second step is the generation of a fracture-local conforming mesh, splitting the triangles of the baseline mesh into polygons conforming to the traces; finally on each fracture F_i, nodes are added on the traces T corresponding to the nodes of the intersecting fracture F_j with $\{i, j\} = \mathcal{I}(T)$, thus gaining global conformity. The three steps are depicted in Figure 4.1 and, the second and third steps are described in full details in the next paragraphs.

4.1.1. Local conformity. Local conformity is obtained as in the previous work [8]. Every time a trace intersects an edge of the triangulation, a new node is created there. Nodes are also created at trace tips. Each trace tip is prolonged up to the nearest edge of the triangulation, thereby creating a new edge and a new node. By doing this, we split the original elements of the triangulation into new "sub-elements", which are elements of the triangulation in their own right. The end result is a mesh of polygonal elements for which all traces are covered by element edges (see Figures 4.1a and 4.1b), with element colouring indicating the number of edges. A careful inspection of those subfigures reveals all of the situations described above.

REMARK 4.1. *An optional mesh modification has been implemented that rearranges some of the nodes of the baseline triangulation before the splitting process, so as to make them coincide with nearby traces, trace tips and trace intersections. This leads to better shaped elements and fewer DOFs for the final mesh and it is not computationally demanding.*

4.1.2. Global conformity. After obtaining the locally conforming mesh the next step is to ensure that all the nodes on the traces are included in the meshes of both fractures that share the trace. These nodes are the ones shared by more than one fracture. This is the most important feature of the method we are proposing and takes full advantage of VEM versatility. Given a trace T shared by fractures F_i and F_j, we define $U_T^{F_i}$ as the set of all nodes on the trace T in fracture F_i and analogously $U_T^{F_j}$ for F_j. The procedure used to obtain the local conforming mesh guarantees that both trace tips are included and that the discretization includes all nodes on the traces and covers it precisely. The complete trace discretization is then $U_T = U_T^{F_i} \cup U_T^{F_j}$. What remains now is to simply add the set of nodes $U_T \setminus U_T^{F_i}$ on the corresponding elements of fracture F_i and analogously for fracture F_j. This can be done since the VEM allows for elements of arbitrary number of edges and 180° angles between them. The final globally conforming mesh is shown in Figure 4.1c and is identical to the previous mesh except for the new added nodes on the traces and a change in element colouring that is an indication of the increment in the number of edges and DOF.

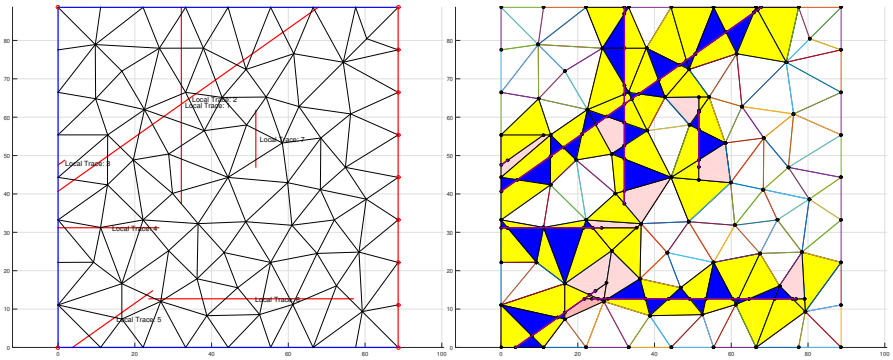

(a) Original (b) Locally conforming

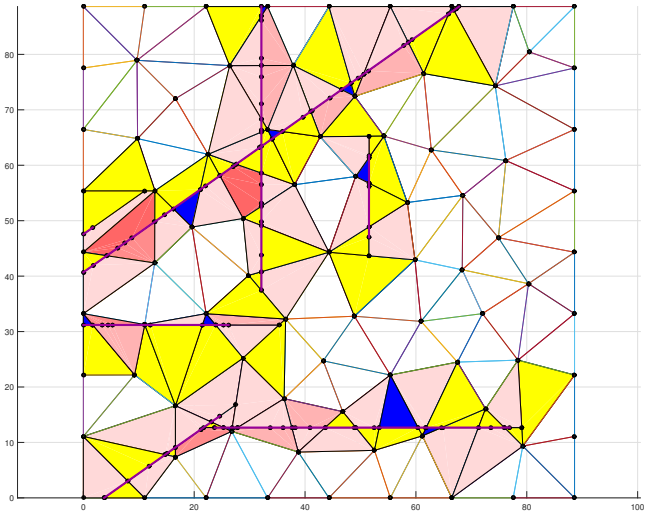

(c) Globally conforming

FIGURE 4.1. *Original mesh, VEM mesh and final globally conforming mesh*

4.2. Imposing matching conditions. For every fracture F_i, with $i = 1, ..., N$, we call n_{dof_i} the number of DOFs of fracture F_i and we assemble the stiffness matrix $K_i \in \mathbb{R}^{n_{dof_i} \times n_{dof_i}}$ following the procedure described in Section 3. Then construct the column vectors $f_i \in \mathbb{R}^{n_{dof_i}}$ as the vector of load values (including terms arising from non-homogeneous boundary conditions) and h_i as the vector of nodal values of the discrete solution. We note that the matrix K_i is singular for fractures with pure Neumann boundary conditions. For the complete DFN we have:

$$K = \begin{pmatrix} K_1 & 0 & \cdots & 0 \\ 0 & K_2 & \cdots & \vdots \\ \vdots & \vdots & \ddots & \vdots \\ 0 & \cdots & \cdots & K_N \end{pmatrix}, \; f = \begin{pmatrix} f_1 \\ \vdots \\ \vdots \\ f_N \end{pmatrix} \text{ and } h = \begin{pmatrix} h_1 \\ \vdots \\ \vdots \\ h_N \end{pmatrix}.$$

In order to obtain the saddle point linear system for the complete DFN we have to impose matching conditions for the nodes on the traces that guarantee the continuity condition of the hydraulic head. We do that by means of Lagrange multipliers λ_t, for

$t = 1, ..., n_{dof_t}$. They are introduced for each node on the traces in a non-redundant way (see [22]) which means that in the case two intersecting traces, i.e. three fractures sharing a single point in space (as in the example on section 5.1.2), only two multipliers are added. To each index $t = 1, \ldots, n_{dof_t}$ corresponds a node on a trace T that is shared by fractures F_i and F_j, and we denote by $dof_i(t)$ the corresponding global DOF for that node on F_i and analogously by $dof_j(t)$ the DOF on F_j. We define $N^h = \sum_{i=1}^{N} n_{dof_i}$, and the row vector $L_t \in \mathbb{R}^{N^h}$ as:

$$L_t = \Big(0 \quad \cdots \quad 0 \quad \overset{dof_i}{1} \quad 0 \quad \cdots \quad 0 \quad \overset{dof_j}{-1} \quad 0 \quad \cdots \quad 0\Big) \tag{4.1}$$

Finally, we set $L \in \mathbb{R}^{n_{dof_t} \times N^h}$ as the matrix:

$$L = \begin{pmatrix} L_1 \\ \vdots \\ \vdots \\ L_{n_{dof_t}} \end{pmatrix}.$$

The final linear system is:

$$\begin{bmatrix} K & L^T \\ L & 0 \end{bmatrix} \begin{bmatrix} h \\ \lambda \end{bmatrix} = \begin{bmatrix} f \\ 0 \end{bmatrix}. \tag{4.2}$$

When the dimensions of the system 4.2 are large, the use of an iterative method and of a preconditioner is advised. We briefly recall the one-level FETI method for domain decomposition as described in [21] here implemented. In this method the primal variables are determined in terms of the Lagrange multipliers. More precisely, we define a block diagonal matrix R as

$$R = \begin{pmatrix} R_1 & 0 & \cdots & 0 \\ 0 & R_2 & \cdots & \vdots \\ \vdots & \vdots & \ddots & \vdots \\ 0 & \cdots & \cdots & R_N \end{pmatrix}$$

where each R_i has a base of the kernel of K_i, $ker(K_i)$ for columns, so that $ker(K) = range(R)$. In the case of the Laplacian operator, R_i corresponds to constant solutions for the subdomains with pure Neumann boundary conditions. Subdomains with Dirichlet boundary conditions have a unique solution and therefore have no contribution for R. It can be shown that

$$h = K^*(f - L^T\lambda) + R\alpha$$

where K^* is the pseudoinverse of K and the vector α depends on λ but not on the primal variables h. This means that if we solve a system for λ, this completely determines the solution. In order to solve this system for λ, a choice of several preconditioners is possible.

We give a brief outline of the procedure to obtain the Dirichlet preconditioner for the one-level FETI, denoted M^{-1}. Let us define $\mathcal{K}^t$ as the sum of transmissivity

values of the fractures that share the node associated with the t degree of freedom. We first multiply the coefficient $(L)_{L_t,dof_i(t)}$ by $\mathcal{K}_i/\mathcal{K}^t$ and the coefficient $(L)_{L_t,dof_j(t)}$ by $\mathcal{K}_j/\mathcal{K}^t$. This takes into account the relative weight of the transmissivity coefficient of each fracture with respect to the sum of the transmissivity coefficients of the fractures associated with that node. In this way we obtain the a matrix L_D. For each fracture we denote by τ the set of fracture DOFs corresponding to nodes placed on the traces, and by ζ the set of the remaining DOFs. Then we can rearrange matrices K_i to obtain:

$$\tilde{K}_i = \begin{bmatrix} K_i^{(\zeta\zeta)} & K_i^{(\tau\zeta)T} \\ K_i^{(\tau\zeta)} & K_i^{(\tau\tau)} \end{bmatrix}.$$

The local Schur complement S_i is

$$S_i = K_i^{(\tau\tau)} - K_i^{(\tau\zeta)}(K_i^{(\zeta\zeta)})^{-1}K_i^{(\tau\zeta)T}.$$

If we define S as the block diagonal Schur complement matrix of the whole system, the Dirichlet preconditioner for the one-level FETI is then

$$M^{-1} = L_D S L_D^T,$$

and its name is a consequence of the fact that for each application of the preconditioner, a local Dirichlet problem has to be solved. The lumped preconditioner is defined similarly as:

$$M^{-1} = L_D K^{(\tau\tau)} L_D^T,$$

where $K^{(\tau\tau)}$ is the block diagonal matrix made up by the local $K_i^{(\tau\tau)}$. We note that in order to define inner products for the pcg FETI algorithm, a symmetric, positive definite matrix Q is used [21]. In our experiments we have considered $Q = M^{-1}$.

5. Numerical results. In this section we present some numerical results, beginning with convergence results for benchmark problems and VEM spaces of various orders, followed by a comparison with a proven method on a medium size DFN. We also exhibit some examples of numerical instabilities arising mainly with the higher order approximation spaces for certain particularly adverse geometrical configurations. All of the results were obtained using a constant transmissivity tensor $\mathcal{K} = 1$.

5.1. Convergence results. The error norms used for the convergence curves are the usual L^2 and H^1 norms. The error is computed by taking the projection of the discrete solution on the space of polynomials, since the values of the discrete solution are only known at the DOFs and are not explicitly known inside the elements (see [6]):

$$Err^2_{L^2} = \sum_{E\in\mathcal{T}_\delta} ||H - \Pi^\nabla_{E,k} h_E||^2_{L^2(E)},$$
$$Err^2_{H^1} = \sum_{E\in\mathcal{T}_\delta} ||H - \Pi^\nabla_{E,k} h_E||^2_{H^1(E)}$$

where $\Pi^\nabla_{E,k}$ is the projection operator of order k as defined in section 3, H is the exact solution and h_E is the discrete solution restricted to element E.

The flux incoming in a fracture trough the traces is computed as the jump of the conormal derivative of the discrete solution over the trace. For every trace we fix a tangential orientation and a normal unitary vector obtained by clockwise rotating by 90 deg the tangent vector of the trace in the fracture plane. For every mesh edge $e \subset T$, i.e. an edge included in trace T, we consider a unique normal vector $\mathbf{n}_{e,i}$ in F_i with an orientation given by the normal vector fixed for the trace, and we define the flux incoming in the fracture F_i trough the edge e, named $u_{e,i}$, as follows:

$$\begin{aligned} u_{left,e,i} &= \nabla \Pi^{\nabla}_{E_l,k} h_{E,i} \cdot \mathbf{n}_{e,i}, \\ u_{right,e,i} &= -\nabla \Pi^{\nabla}_{E_r,k} h_{E,i} \cdot \mathbf{n}_{e,i}, \\ u_{e,i} &= u_{left,e,i} + u_{right,e,i}, \end{aligned}$$

where E_l and E_r are the elements to the left and to the right of the trace that share the edge e, respectively.

The flux entering in the fracture F_i through trace T is then obtained by repeating this procedure over all the mesh edges in F_i belonging to T:

$$u_{T,i} = \sum_{e \subset T} u_{e,i}.$$

The L2 error of the flux on the trace is then:

$$ErrU^2_{L^2} = ||U_{T,i} - u_{T,i}||^2_{L^2(T)},$$

where $U_{T,i}$ is the exact incoming flux in F_i through trace T.

5.1.1. Benchmark problem 1. This first problem has been considered before in the context of the XFEM (eXtended finite elements) [10] and of the VEM [8] as a single-fracture problem. Nevertheless, it remains interesting for the fact that it includes a trace tip inside the domain and the exact solution is known. In this work the problem is considered as a 2-fracture DFN, as shown in Figure 5.1 and the error calculations and convergence curves are shown for the first fracture, F_1.

Let us define the domains F_1 and F_2 as

$$\begin{aligned} F_1 &= \left\{(x,y,z) \in \mathbb{R}^3 : -1 \le x \le 1,\ -1 \le y \le 1,\ z = 0\right\}, \\ F_2 &= \left\{(x,y,z) \in \mathbb{R}^3 : -1 \le x \le 0,\ -1 \le z \le 1,\ y = 0\right\}, \end{aligned}$$

with a single trace $T = \left\{(x,y) \in \mathbb{R}^3 : y = 0, z = 0 \text{ and } -1 \le x \le 0\right\}$ ending in the interior of F_1 (Figure 5.1).

Exact solutions for F_1 and F_2 are given by $H^{ex}_1(x,y)$ and $H^{ex}_2(x,y)$:

$$\begin{aligned} H^{ex}_1(x,y,z) &= -\cos\left(\frac{1}{2}\arctan2(x,y)\right)(x^2-1)(y^2-1)(x^2+y^2) \\ H^{ex}_2(x,y,z) &= -\cos\left(\frac{1}{2}\arctan2(x,y)\right)(z^2-1)(x^2-1)(z^2+x^2) \end{aligned}$$

where $\arctan2(x,y)$ is the arc-tangent function with 2 arguments, that returns the appropriate quadrant of the computed angle.

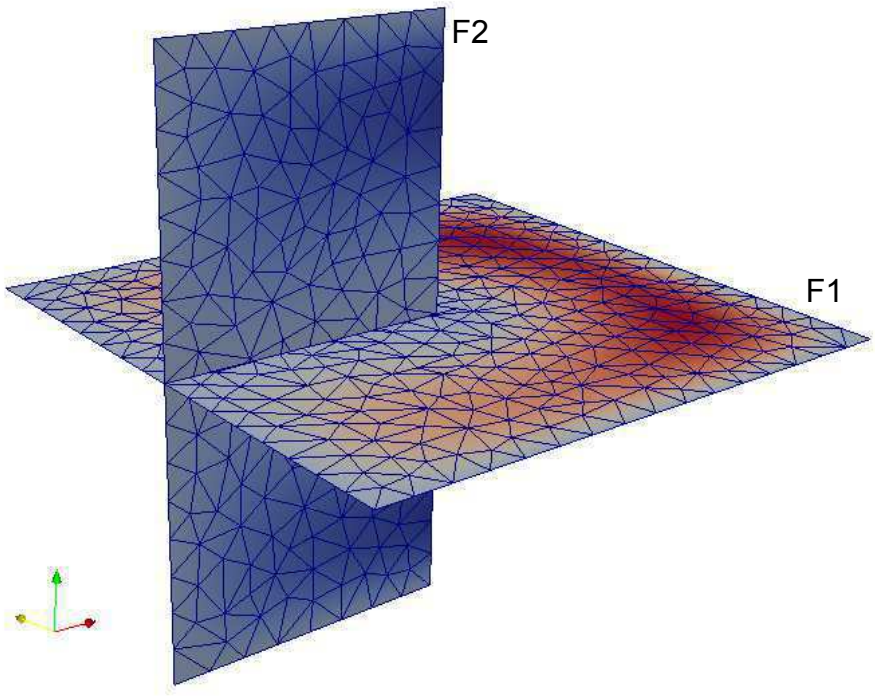

FIGURE 5.1. *Spatial distribution of fractures for benchmark problem 1*

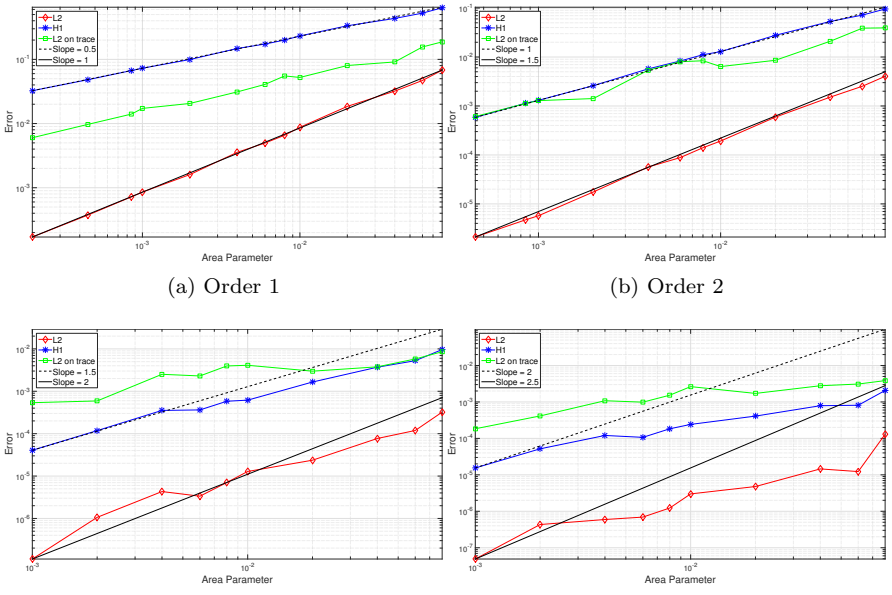

(a) Order 1 (b) Order 2

(c) Order 3 (d) Order 4

FIGURE 5.2. *Convergence curves for benchmark problem 1 - Fracture 1*

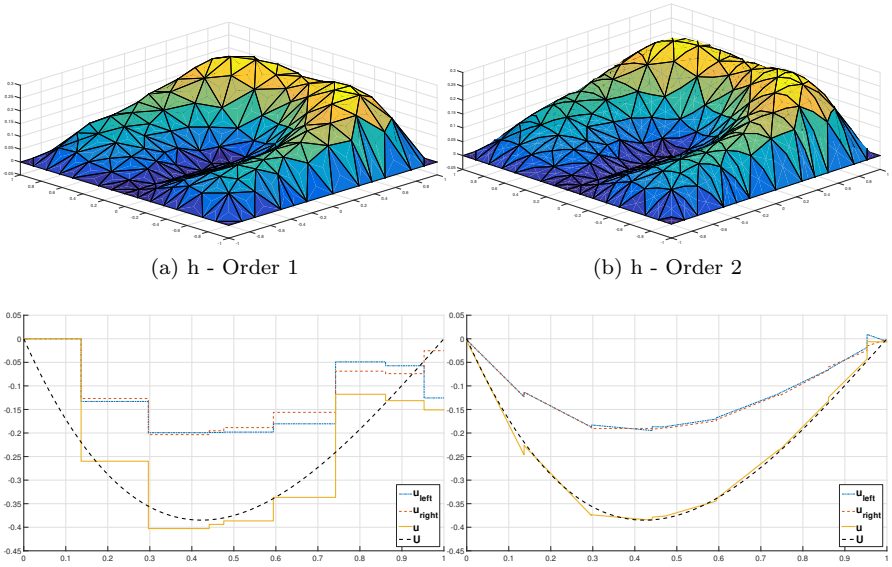

(a) h - Order 1 (b) h - Order 2

(c) u - Order 1 (d) u - Order 2

FIGURE 5.3. *Solutions for benchmark problem 1 - Fracture 1*

The problem is then:

$$\begin{aligned} -\Delta H &= -\Delta H_1^{ex} \text{ on } F_1 \setminus T, \\ H &= 0 \text{ on } \partial F_1, \end{aligned}$$

$$\begin{aligned} -\Delta H &= -\Delta H_2^{ex} \text{ on } F_2 \setminus T, \\ H &= (z^2 - z^4)\cos(\pi/4) \text{ on } \partial F_2^D \\ H &= 0 \text{ on } \partial F_2 \setminus \partial F_2^D. \end{aligned}$$

where $\partial F_2^D = \left\{(x, y, z) \in \mathbb{R}^3 : x = 0, y = 0, -1 \leq z \leq 1\right\}$ is the boundary of F_2 with non-homogeneous Dirichlet boundary conditions.

Convergence curves for the VEM of orders from 1 to 4 are shown in Figure 5.2. The expected rates of convergence are obtained for orders 1 and 2, whereas a slower rate of convergence for orders 3 and 4 was obtained as a consequence of the insufficient regularity of the exact solution in the sense of Sobolev spaces.

Numerical solutions for the hydraulic head H_1 with the VEM of orders 1 and 2 are shown in Figure 5.3 a) and b). In Figure 5.3 c) and d), we present a comparison between the exact solution and the approximate solution of the flux incoming in F_1, as well as its left and right components. Note how the approximation of the the trace flux U is piecewise constant for order 1 VEM and piecewise linear for order 2 VEM, and the approximation of the exact flux (dashed line) with the VEM of second order is greatly improved.

5.1.2. Benchmark problem 2. This problem shows the performance of the proposed approach in presence of trace intersections. The considered system consists of 3 fractures and 3 traces as shown in Figure 5.4:

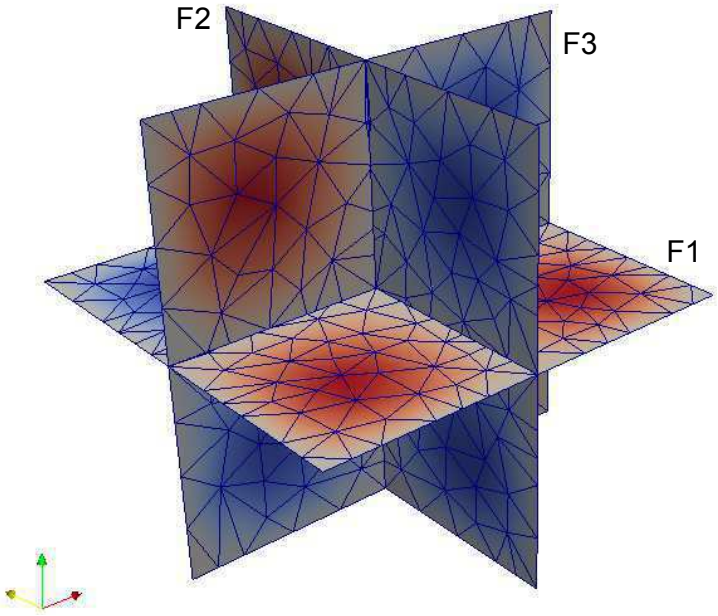

FIGURE 5.4. *Spatial distribution of fractures for benchmark problem 2*

$$
\begin{aligned}
F_1 &= \left\{(x,y,z) \in \mathbb{R}^3 : -1 \le x \le 1,\ -1 \le y \le 1,\ z = 0\right\},\\
F2 &= \left\{(x,y,z) \in \mathbb{R}^3 : -1 \le y \le 1,\ -1 \le z \le 1,\ x = 0\right\},\\
F3 &= \left\{(x,y,z) \in \mathbb{R}^3 : -1 \le z \le 0,\ -1 \le x \le 1,\ y = 0\right\},
\end{aligned}
$$

$$
\begin{aligned}
T1 &= \left\{(x,y,z) \in \mathbb{R}^3 : -1 \le x \le 1,\ y = 0,\ z = 0\right\},\\
T2 &= \left\{(x,y,z) \in \mathbb{R}^3 : -1 \le y \le 1,\ z = 0,\ x = 0\right\},\\
T3 &= \left\{(x,y,z) \in \mathbb{R}^3 : -1 \le z \le 0,\ x = 0,\ y = 0\right\}.
\end{aligned}
$$

Note that all of three traces intersect in a single point $P = (0,0,0)$ in space (as it is always the case for the intersection of 3 planar fractures).

Exact solutions are known for all fractures:

$$
\begin{aligned}
H_1^{ex}(x,y) &= |x|(1+x)(1-x)y(1+y)(1-y),\\
H_2^{ex}(y,z) &= y(1+y)(1-y)|z|(1+z)(1-z),\\
H_3^{ex}(z,x) &= z(1+z)(1-z)x(1+x)(1-x).
\end{aligned}
$$

Note that H_1^{ex} and H_2^{ex} are not C^1 in the whole fracture, but, for each of the 4 subdomains defined by the traces in each fracture, they are in fact polynomials of degree 6.

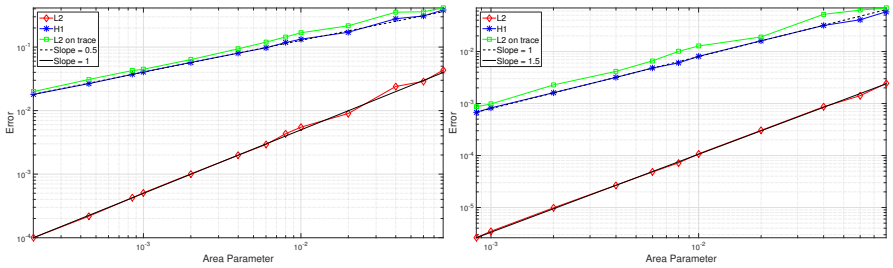

(a) Order 1

(b) Order 2

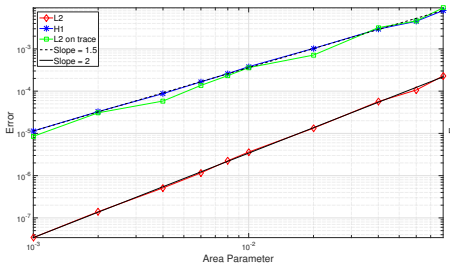

(c) Order 3

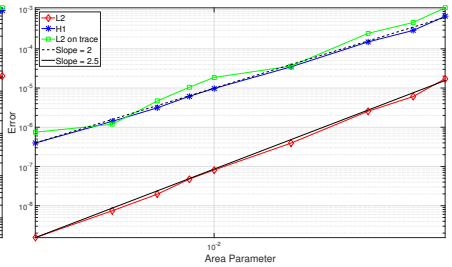

(d) Order 4

FIGURE 5.5. *Convergence curves for benchmark problem 2 - Fracture 1*

TABLE 5.1
Net flux in source and sink fractures.

Method	150			120			90			60		
	Si	So	Δ	Si	So	Δ	Si	So	Δ	Si	So	Δ
VEM-1	8.75	-8.22	0.53	8.70	-7.92	0.78	9.01	-7.75	1.26	9.73	-8.32	1.42
VEM-2	11.23	-9.78	1.45	11.16	-10.05	1.09	11.18	-10.03	1.08	11.40	-10.26	1.14
VEM-3	11.60	-10.36	1.23	11.64	-10.60	1.04	11.64	-10.73	0.91	11.80	-10.89	0.91
VEM-4	11.88	-10.76	1.12	11.89	-10.92	0.98	11.91	-10.99	0.92	12.03	-11.17	0.86
	30			15			10			5		
	Si	So	Δ	Si	So	Δ	Si	So	Δ	Si	So	Δ
VEM-1	10.56	-8.51	2.05	10.71	-9.49	1.23	10.98	-9.18	1.81	11.36	-10.26	1.12
VEM-2	11.83	-10.77	1.06	11.91	-11.00	0.91	12.00	-11.09	0.90	12.12	-11.65	0.47
VEM-3	12.11	-11.25	0.86	12.13	-11.53	0.59	-	-	-	-	-	-
VEM-4	12.26	-11.48	0.78	10.21	-13.01	-2.81	-	-	-	-	-	-

The problem is then:

$$
\begin{aligned}
-\Delta H &= 6|x|y(x^2+y^2-2) \text{ on } F_1 \setminus T_1,\\
-\Delta H &= 6|y|z(y^2+z^2-2) \text{ on } F_2 \setminus T_2,\\
-\Delta H &= 6zx(z^2+y^2-2) \text{ on } F_3 \setminus T_3,\\
H &= 0 \text{ on } \partial F_1 \cup \partial F_2 \cup \partial F_3.
\end{aligned}
$$

Convergence curves for the VEM of orders from 1 to 4 are shown in Figure 5.5 and solutions for order 1 and 2 are reported in Figure 5.6. In contrast with benchmark problem 1, the expected convergence speed is achieved for all orders, since now the exact solution has C^∞ regularity on each sub-fracture thanks to the local conformity of the mesh. The error in the discrete solution for the order 6 discretization is $||H-h||^2_{L^2} = 3.53e{-}19$, $||\partial_x(H-h)||^2_{L^2} = 5.09e{-}18$ and $||\partial_y(H-h)||^2_{L^2} = 5.85e{-}18$, being then of the same order of the round-off error in double precision. This confirms that the discrete solution coincides numerically with the exact solution.

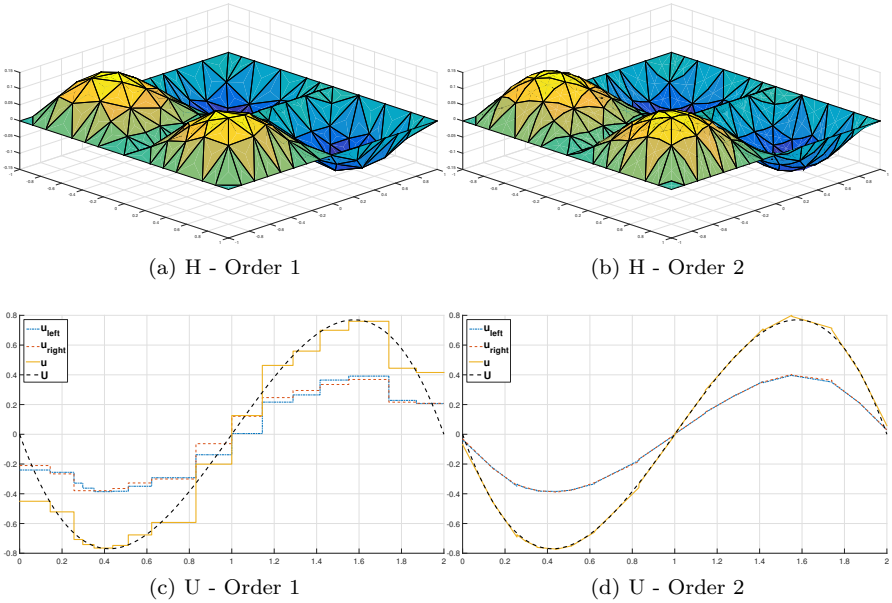

(a) H - Order 1 (b) H - Order 2

(c) U - Order 1 (d) U - Order 2

FIGURE 5.6. *Solutions for benchmark problem 2 - Fracture 1 and trace 1*

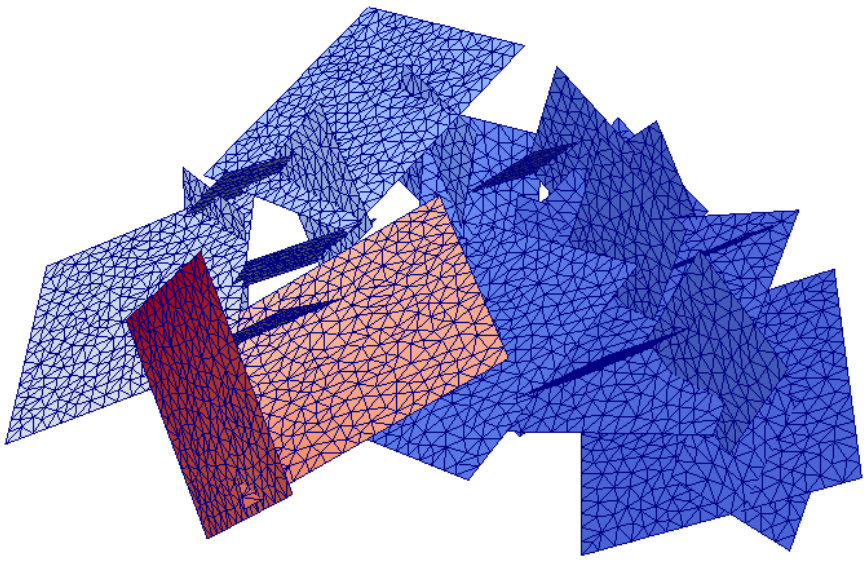

FIGURE 5.7. *Spatial distribution of fractures for a DFN with 27 fractures*

5.2. DFN - 27 fractures. Let us consider the DFN shown in Figure 5.7 consisting of 27 fractures. A sink fracture F_1 and a source fracture F_2 are defined, both having a non homogeneous Dirichlet boundary conditions on one edge of their boundary and homogeneous Neumann boundary conditions on the remaining edges. All other fractures have homogeneous Neumann boundary conditions and are there-

TABLE 5.2
Comparison of iterations for different choices of Q and preconditioner M^{-1}

			$\mathbb{I}$	Lumped	Dirichlet
Method/Area	Total DOF	Trace DOF	Iter	Iter	Iter
VEM-1/150	7209	2047	137	106	72
VEM-1/90	9220	2524	152	118	77
VEM-1/30	19116	4182	29891	138	80
VEM-1/5	75672	9833	NC	238	113
VEM-2/150	25028	3869	181	259	77
VEM-2/90	34038	4823	4537	286	74
VEM-2/30	79736	8139	NC	357	112

fore insulated on their boundaries. In absence of an exact solution, the difference Δ between the flux entering the system from F_2 (the source fracture) and the flux leaving it from F_1 (sink fracture), is considered for assessing the quality of the obtained numerical approximation.

It should be noted that the methodology presented in this work does not guarantee nor aims to have local mass conservation in each fracture, since this is not explicitly imposed on any fracture. This means that the global mass conservation is well described, but the "local" flux balances (i.e., on each individual fracture) can be somewhat less accurate. On the other hand, these fracture flux balances are expected to improve with finer meshes as the method is converging to the solution. On the whole, the method can be seen as basically solving the DFN problem in one very complex 3D domain in space, that may however still be thought as a 2D domain.

Table 5.2 shows the net flux in the source and sink fractures, as well as the difference Δ for various mesh parameters and orders of the VEM space.

After extensive numerical experiments a trend emerged in the results; for order 1, convergence can be quite slow in the flux variable, and can be attributed to the fact that the approximation is only piecewise constant and the projection of the VEM space functions for each element is onto a polynomial space of degree 1, regardless of the number of edges of the element. Moving to higher order discretization spaces, the approximation of the flux improves. A marked improvement is obtained with second order VEM with respect to the first order, probably due to the piecewise linear structure of U. Further increasing the VEM order has a less noticeable effect, with practically no gain in moving to a third or fourth order approximation. In addition, higher order discretizations might suffer from numerical instabilities due to very badly shaped elements. This is for example the case for the fourth order approximation on the mesh size 15, where instabilities cause a degenerate discrete solution as shown by the parameter Δ reported in Table 5.2. Further details on possible causes of instabilities are discussed later in Paragraph 5.4.

REMARK 5.1. *When tackling a new DFN, a good practice would be to run it the first time with a coarse mesh and first order elements. The values of h and of u already provide a reliable indication of the order of magnitude of the correct solution, and using the flux values on each fracture one can establish a rule for selecting the fractures for which a mesh refinement is advisable. Fractures with less important contribution to the total flux through the DFN do not require a finer mesh. Afterwards, a new simulation can be launched with second order elements and the new adapted mesh.*

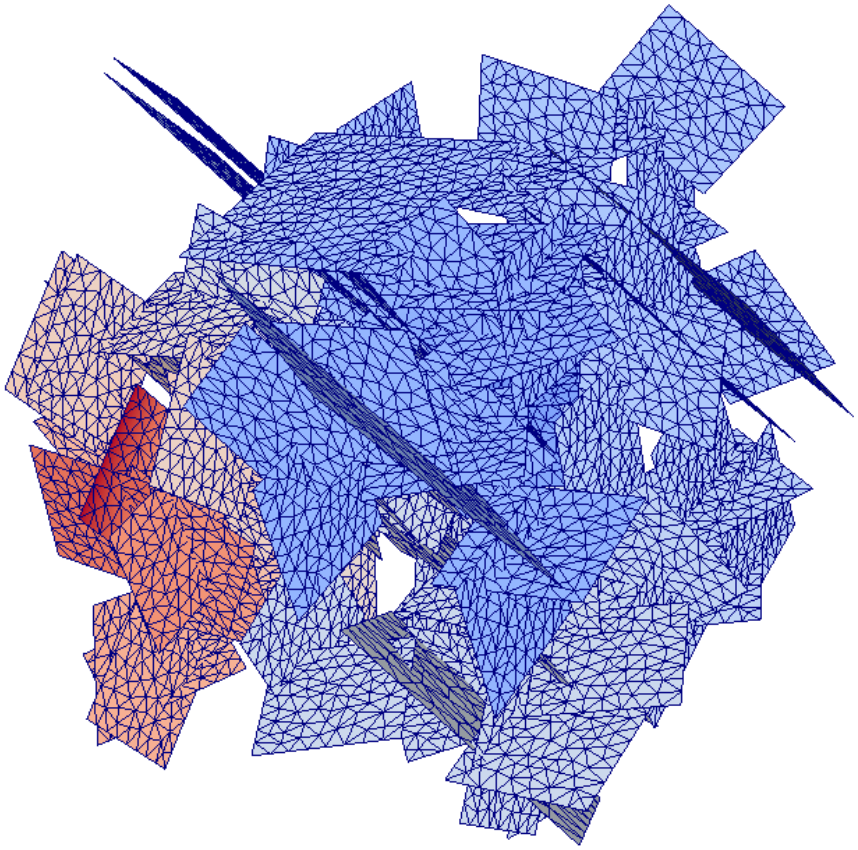

FIGURE 5.8. *Spatial distribution of fractures for a DFN with 120 fractures*

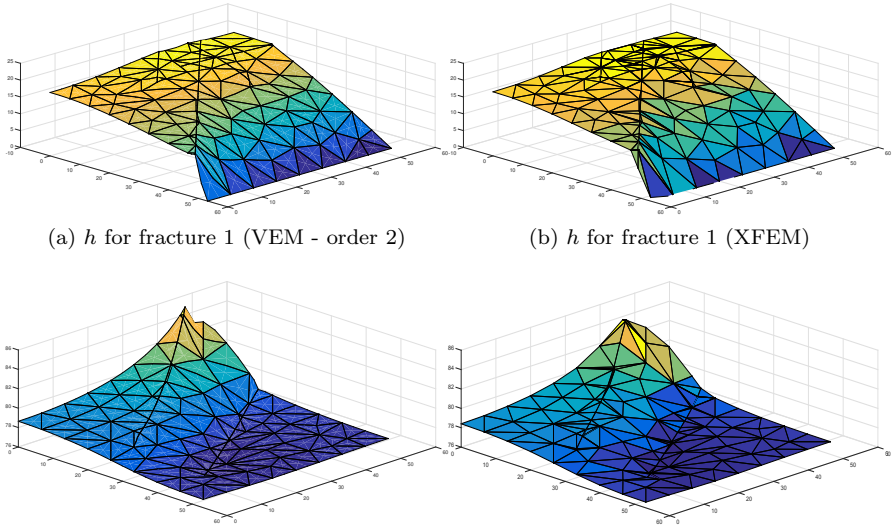

(a) h for fracture 1 (VEM - order 2)

(b) h for fracture 1 (XFEM)

(c) h for fracture 57 (VEM - order 2)

(d) h for fracture 57 (XFEM)

FIGURE 5.9. *Large DFN comparison*

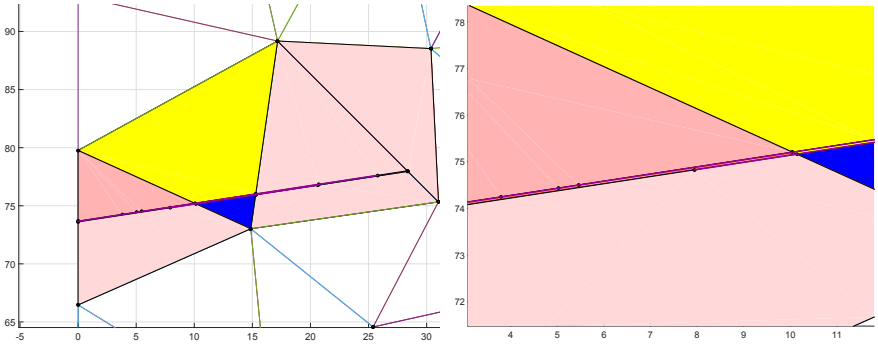

(a) Mesh (b) Detail

FIGURE 5.10. *Detail of two very close and almost parallel traces*

5.3. DFN - 120 fractures. We now consider a DFN consisting of 120 fractures, as seen in Figure 5.8. Dirichlet boundary conditions are imposed on a source and sink fracture whereas all other fractures have homogeneous Neumann boundary conditions. In Figure 5.9 we show the solution for the sink fracture and for a selected fracture with insulated boundaries. As a comparison, results are shown for both the VEM approach of order 2 depicted in the present work and for an eXtended Finite Element Method (XFEM) based optimization approach described in [11], starting from the same baseline mesh. A very good agreement between the solutions can be appreciated in the figure. Good agreement was also obtained for VEM of orders 1 and 3.

In Table 5.2, we report the behaviour of 2 preconditioning techniques. Different mesh parameters and VEM of order 1 and 2 are considered. The table displays the number of iterations required by the non preconditioned pcg routine compared to the performances of the preconditioned algorithm with the Lumped and Dirichlet preconditioners. In the first case, a rapid increase in the iteration number with mesh refinement can be appreciated for both orders 1 and 2. As expected, the increase in iterations with a preconditioner is much smaller, with the Dirichlet preconditioner performing better than the Lumped preconditioner.

The notable improvement renders almost imperative the use of a preconditioner, since the reduction in iteration number far outweighs the extra computational cost that arises from the computation of the preconditioner. Cases marked with NC stand for no convergence after 1 million iterations.

5.4. A survey of troublesome situations. In this subsection we describe some situations arisen in the simulations that have proven to be difficult to handle numerically. The monomial base for the space of polynomials is notoriously bad conditioned, and the situation worsens with increasing orders. We believe that this is the cause of the issues we are presenting in this section, and they arise in elements with unsuitable shapes. Some of these issues can be prevented if a mesh modifying procedure as mentioned in Remark 4.1 is used.

A first example is related to the DFN with 120 fractures, where a fracture has two traces that are almost parallel and very close to each other, as in Figure 5.10. This inevitably leads to elements with a bad aspect ratio, since any attempt to obtain an adequate mesh would require a very large number of small elements to fill the space between the two traces. The solution is stable up to VEM of order 3, while

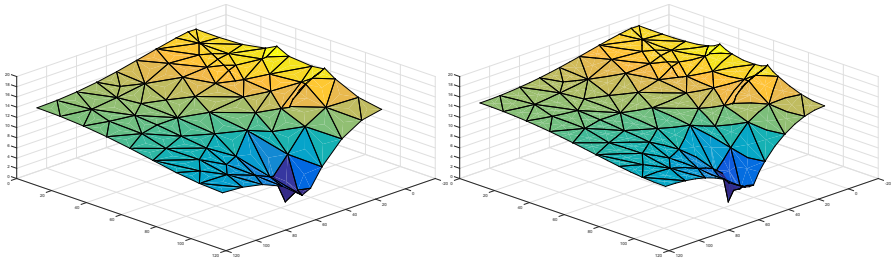

(a) Order 1 (b) Order 2

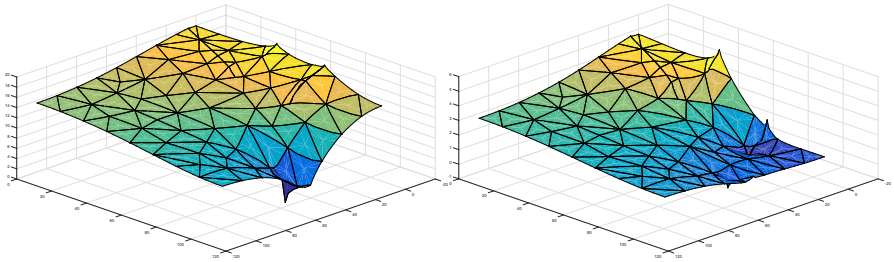

(c) Order 3 (d) Order 4

FIGURE 5.11. *Comparison of results for problematic situations*

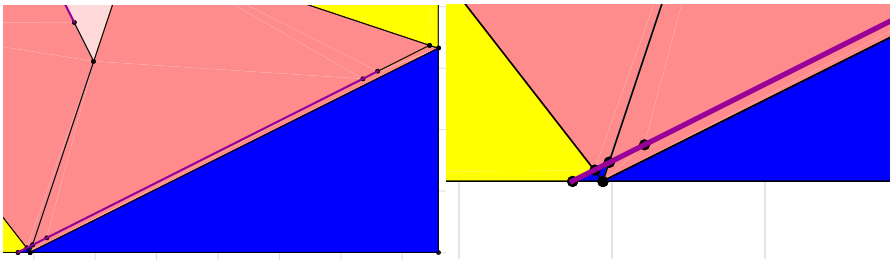

(a) Mesh (b) Detail

FIGURE 5.12. *Detail of two very close and almost parallel traces*

when using a fourth order approximation the obtained solution drastically changes (see Figure 5.11), and even falls below zero, which is impossible since we have Dirichlet boundary conditions between 0 and 100 and this necessarily leads to a solution between those values for all fractures. As a reference, one particularly problematic mesh element has an almost rectangular shape and an area of 0.58, with a length of 10.26 in one direction and 0.058 in the other (a 177 ratio). This is a degenerate octagon and for order 4 it has 38 DOFs (Figure 5.10). We remark that this particular configuration can be successfully dealt with VEM of orders from 1 to 3, and problems only appear with order 4 and higher.

A second documented problematic configuration concerns badly shaped elements due not to the geometry of the DFN but to an unfortunate mesh parameter, and is such that it may not be present with either a finer or a coarser mesh. The situation is depicted in Figure 5.12, where we can see that the edge of an element is very close to a trace and has originated elements much more stretched in one direction than in

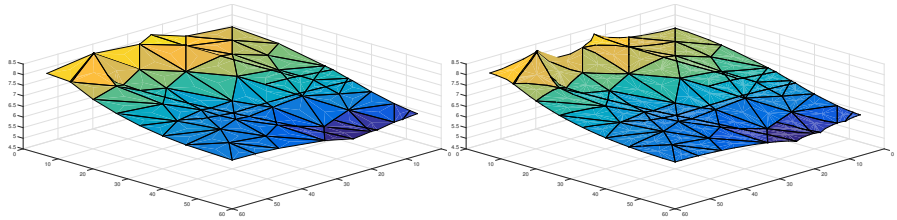

(a) Order 1 (b) Order 3

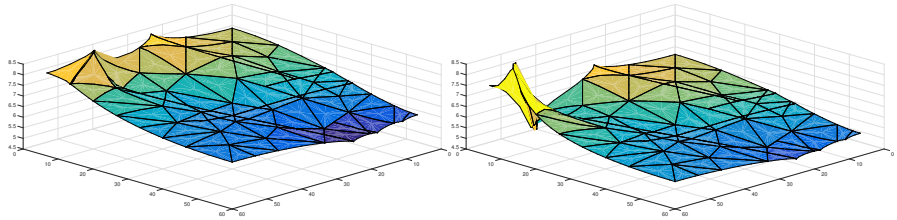

(c) Order 4 (d) Order 5

FIGURE 5.13. *Comparison of results for problematic situations*

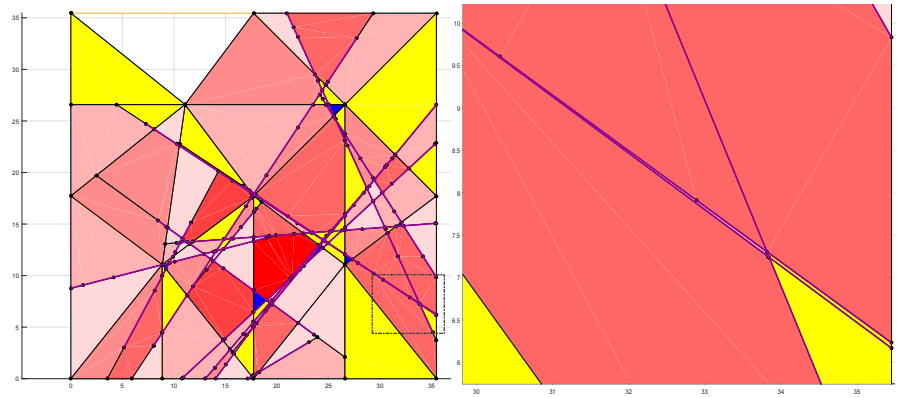

(a) Mesh (b) Detail

FIGURE 5.14. *Detail of two traces meeting at a very small angle*

the other. Furthermore, a very small element was generated next to the stretched element. The solution for order 5 VEM becomes numerically unstable in this case, as shown by Figure 5.13. We remark that the major source of instability in this case is again the elongated element and not the neighboring small element.

Finally, we present the last case that is part of a medium size DFN (130 fractures) that includes parallel traces very close to each other, large disparity between trace lengths, highly heterogeneous element areas, element angles of less than 1 degree and complex trace intersections among other complications. More precisely, we have for the whole DFN that: $Area_{max}/Area_{min} \approx 2.10^9$, minimum angle $= 0.41°$, maximum trace length ≈ 45, minimum trace length ≈ 0.01 and largest number of traces in a fracture $= 24$. An adequate globally conforming mesh for this system would be quite difficult to obtain, if not impossible. With our approach, meshing can be done as

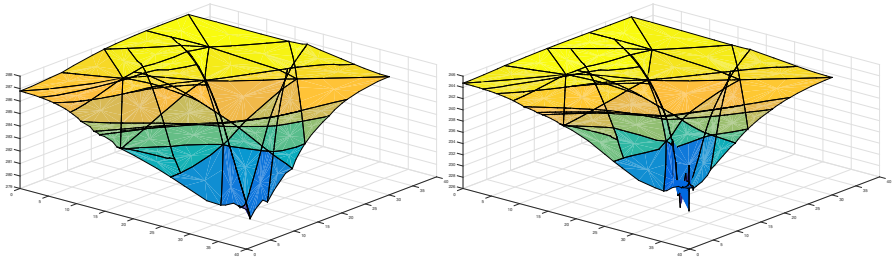

(a) Order 3 (b) Order 4

FIGURE 5.15. *Comparison of results for problematic situations*

usual (Figure 5.14) although it may lead to elements with undesirable shapes. It can be seen that irregularities in the solution were present starting from VEM of order 4, again at a very elongated element between two traces meeting at a very small angle (Figure 5.15). The solution shows an uneven and rough behavior that is further propagated to other fractures that have traces in common, and was not present for VEM of order 3.

6. Conclusions. In this work we have presented a novel method that constitutes a natural generalization of conforming Finite Elements for Discrete Fracture Network flow simulations. Local and global conformity is obtained using some of the features of the Virtual Element Method, and most importantly, global conformity is achieved without any constraints in the meshing process, that is performed independently for each fracture, nor any modification of DFN geometry. Convergence curves were presented as well as results for DFNs of small and medium scale, and the method has been shown to be robust enough to handle complex geometrical situations that arise in randomly generated DFNs.

After extensive numerical experiments, the following patterns were noticed: in general, all methods give a good approximation for H, and due to how the problem was implemented, continuity of H for the whole DFN is guaranteed. Even with VEM of order 1 the solutions are reliable for this variable, and this is due to the fact that we are using the primal formulation of the problem and the local conformity of the mesh allows for a more accurate representation of the jump of the derivative of H along the traces. In the case of U, the situation is different; only starting with a somewhat fine mesh can acceptable results be obtained for order 1. Order 2 on the other hand, shows a marked improvement that can be attributed to the larger number of DOF but also to the improved approximation of the gradient of H (i.e., U). We remark that U is not obtained directly, but derived from the projection onto a polynomial space of the primal variable H.

Concerning the use of discretizations with increasing polynomial accuracy, for this application, we discourage going beyond order 2 based on the obtained results. Higher orders are not only less stable numerically on strongly distorted meshes, but also much more computationally expensive, and the improvement in accuracy is often not considerable. In fact, the exact solution of a DFN does not have in general high regularity and a cubic approximation of H and a quadratic approximation for U might be excessive. As we have seen however, whenever regularity is guaranteed, convergence for higher orders is as good as expected.

FETI algorithms for domain decomposition were successfully implemented and

show promise for possible parallelization of the resulting linear system. They prove to be nearly indispensable if a large system is to be solved due to the achievable reduction in the number of iterations required to solve the system.

Finally, much of the work done here in obtaining the globally conforming meshes as well as the idea for imposing matching conditions between corresponding degrees of freedom can be readily applied with few alterations to an implementation of a mixed formulation of the original problem using mixed Virtual Elements and will the subject of future work.

REFERENCES

[1] P. M. Adler, *Fractures and Fracture Networks*, Kluwer Academic, Dordrecht, 1999.

[2] B. Ahmad, A. Alsaedi, F. Brezzi, L. D. Marini, and A. Russo, *Equivalent projectors for virtual element methods*, Comput. Math. Appl., 66 (2013), pp. 376–391.

[3] P. F. Antonietti, L. B. da Veiga, D. Mora, and M. Verani, *A stream virtual element formulation of the stokes problem on polygonal meshes*, SIAM Journal on Numerical Analysis, 52 (2014), pp. 386–404.

[4] F. Beirão da Veiga, L. Brezzi, L. D. Marini, and A. Russo, *The hitchhikers guide to the virtual element method*, Mathematical Models and Methods in Applied Sciences, 24 (2014), pp. 1541–1573.

[5] L. Beirão da Veiga, F. Brezzi, A. Cangiani, G. Manzini, L. D. Marini, and A. Russo, *Basic principles of virtual element methods*, Math. Models Methods Appl. Sci., 23 (2013), pp. 199–214.

[6] L. Beirão da Veiga, F. Brezzi, L. D. Marini, and A. Russo, *Virtual element methods for general second order elliptic problems on polygonal meshes*, SUBMITTED, preprint 2014arXiv1412.2646B.

[7] L. Beirão da Veiga and G. Manzini, *A virtual element method with arbitrary regularity*, IMA Journal of Numerical Analysis, 34 (2014), pp. 759–781.

[8] M. F. Benedetto, S. Berrone, S. Pieraccini, and S. Scialò, *The virtual element method for discrete fracture network simulations*, Computer Methods in Applied Mechanics and Engineering, 280 (2014), pp. 135 – 156.

[9] S. Berrone, S. Pieraccini, and S. Scialò, *A PDE-constrained optimization formulation for discrete fracture network flows*, SIAM J. Sci. Comput., 35 (2013), pp. B487–B510.

[10] S. Berrone, S. Pieraccini, and S. Scialò, *On simulations of discrete fracture network flows with an optimization-based extended finite element method*, SIAM J. Sci. Comput., 35 (2013), pp. A908–A935.

[11] S. Berrone, S. Pieraccini, and S. Scialò, *An optimization approach for large scale simulations of discrete fracture network flows*, J. Comput. Phys., 256 (2014), pp. 838–853.

[12] F. Brezzi and L. D. Marini, *Virtual element methods for plate bending problems*, Computer Methods in Applied Mechanics and Engineering, 253 (2013), pp. 455 – 462.

[13] M. C. Cacas, E. Ledoux, G. de Marsily, B. Tillie, A. Barbreau, E. Durand, B. Feuga, and P. Peaudecerf, *Modeling fracture flow with a stochastic discrete fracture network: calibration and validation: 1. the flow model*, Water Resour. Res., 26 (1990), pp. 479–489.

[14] A. Cangiani, G. Manzini, A. Russo, and N. Sukumar, *Hourglass stabilization and the virtual element method*, International Journal for Numerical Methods in Engineering, (2014).

[15] L. B. da Veiga, F. Brezzi, and L. D. Marini, *Virtual elements for linear elasticity problems*, SIAM Journal on Numerical Analysis, 51 (2013), pp. 794–812.

[16] B. Decroux and O. Gosselin, *Computation of effective dynamic properties of naturally fractured reservoirs: Comparison and validation of methods*, Society of Petroleum Engineers, 2013.

[17] W. S. Dershowitz and C. Fidelibus, *Derivation of equivalent pipe networks analogues for three-dimensional discrete fracture networks by the boundary element method*, Water Resource Res., 35 (1999), pp. 2685–2691.

[18] J. Erhel, J.-R. De Dreuzy, and B. Poirriez, *Flow simulation in three-dimensional discrete fracture networks*, SIAM Journal on Scientific Computing, 31 (2009), pp. 2688–2705.

[19] C. Fidelibus, G. Cammarata, and M. Cravero, *Hydraulic characterization of fractured rocks. In: Abbie M, Bedford JS (eds) Rock mechanics: new research.*, Nova Science Publishers Inc., New York, 2009.

[20] T. Kalbacher, R. Mettier, C. McDermott, W. Wang, G. Kosakowski, T. Taniguchi,

and O. Kolditz, *Geometric modelling and object-oriented software concepts applied to a heterogeneous fractured network from the grimsel rock laboratory*, Comput. Geosci., 11 (2007), pp. 9–26.

[21] A. Klawonn, *FETI domain decomposition methods for second order elliptic partial differential equations*, GAMM-Mitteilungen, 29 (2006), pp. 319–341.

[22] A. Klawonn and O. Widlund, *FETI and Neumann-Neumann iterative substructuring methods: Connections and new results*, Comm. Pure Appl. Math., 54 (2001), pp. 57–90.

[23] V. Lenti and C. Fidelibus, *A BEM solution of steady-state flow problems in discrete fracture networks with minimization of core storage*, Computers & Geosciences, 29 (2003), pp. 1183 – 1190.

[24] S. Li, Z. Xu, G. Ma, and W. Yang, *An adaptive mesh refinement method for a medium with discrete fracture network: The enriched perssons method*, Finite Elements in Analysis and Design, 86 (2014), pp. 41 – 50.

[25] J. Maryška, O. Severỳn, and M. Vohralík, *Numerical simulation of fracture flow with a mixed-hybrid fem stochastic discrete fracture network model*, Computational Geosciences, 8 (2005), pp. 217–234.

[26] P. Panfili and A. Cominelli, *Simulation of miscible gas injection in a fractured carbonate reservoir using an embedded discrete fracture model*, in Proceedings of Abu Dhabi International Petroleum Exhibition and Conference, SPE International, 2014.

[27] G. Pichot, J. Erhel, and J. de Dreuzy, *A mixed hybrid mortar method for solving flow in discrete fracture networks*, Applicable Analysis, 89 (2010), pp. 1629–1643.

[28] ———, *A generalized mixed hybrid mortar method for solving flow in stochastic discrete fracture networks*, SIAM Journal on scientific computing, 34 (2012), pp. B86–B105.

[29] M. Vohralík, J. Maryška, and O. Severýn, *Mixed and nonconforming finite element methods on a system of polygons*, Applied Numerical Mathematics, 51 (2007), pp. 176–193.